Journal of
Synchrotron Radiation

ISSN 0909-0495

Received 20 February 2012
Accepted 15 May 2012

The dedicated high-resolution grazing-incidence X-ray scattering beamline 8-ID-E at the Advanced Photon Source

Zhang Jiang, Xuefa Li,‡ Joseph Strzalka, Michael Sprung,¶ Tao Sun, Alec R. Sandy, Suresh Narayanan, Dong Ryeol Lee§ and Jin Wang*

X-ray Science Division, Argonne National Laboratory, Argonne, IL 60439, USA.
E-mail: wangj@aps.anl.gov

As an increasingly important structural-characterization technique, grazing-incidence X-ray scattering (GIXS) has found wide applications for *in situ* and real-time studies of nanostructures and nanocomposites at surfaces and interfaces. A dedicated beamline has been designed, constructed and optimized at beamline 8-ID-E at the Advanced Photon Source for high-resolution and coherent GIXS experiments. The effectiveness and applicability of the beamline and the scattering techniques have been demonstrated by a host of experiments including reflectivity, grazing-incidence static and kinetic scattering, and coherent surface X-ray photon correlation spectroscopy. The applicable systems that can be studied at 8-ID-E include liquid surfaces and nanostructured thin films.

Keywords: X-ray scattering; grazing incidence; coherence; beamline; high resolution.

1. Introduction

Complex nanocomposites, especially those highly ordered and composed of organic and inorganic components, have found wide applications in novel electronic, magnetic and photonic devices. Although highly ordered structures in these nanocomposite systems can often form in a self-assembled fashion, the formation of the structures can be extremely dynamic, and far from equilibrium conditions even at the end of the ordering processes. Therefore, controlled self-assembly of nanostructures has to be guided by a thorough understanding of ordering kinetics and nanoparticle dynamics in the complex matrices. By directly probing, in real time, the surface and buried structures in such dynamic systems, many surface- and interface-sensitive characterization techniques provide insight that reveals the mechanisms responsible for the formation and stability of ordered nanostructures. Grazing-incidence small-angle (GISAXS) and wide-angle (GIWAXS) X-ray scattering, because of their probing wave vector range, q, of 10^{-3}–$10\ \mathrm{nm}^{-1}$, which translates to a real-space length scale ranging from 0.1 nm to 1 μm, and temporal resolution of 10^{-3}–1 s, have become increasingly important in characterizing nanostructures and nanocomposites and their formation at surfaces and interfaces in real time and under real conditions. The nature of the grazing-incidence techniques makes them particularly suitable for nanocomposites in ultrathin-film forms.

With the aim of satisfying the increasing need for grazing-incidence X-ray scattering (GIXS), several beamlines have been or are being built at synchrotron radiation facilities around the world. A primary design goal of most of these beamlines is flux, where microfocusing of the X-ray beam is often used to achieve high intensity and a small beam spot. Focusing, however, often leads to a degradation of reciprocal-space resolution, so that most of these beamlines are only well suited for systems that do not have long-range in-plane correlations between nanostructures, such as supported quantum dot growth and phase-separation-induced self-assembly of block copolymers in thin films. In fact, there has been considerable recent progress in producing surface structures with ultra-dense arrays of nanoscopic elements that are highly ordered over macroscopic length scales, for example, templated self-assembly of diblock copolymers (Stein *et al.*, 2007*a*; Park *et al.*, 2009). Another example is the evaporation-driven assembly of metal nanoparticles which have been demonstrated to form long-range-ordered two-dimensional (2D) superlattice domains of sizes up to a micrometer (Jiang *et al.*, 2010*b*). Yet another example is virus-like nanoparticles, such as bacteriophages that are naturally perfectly monodisperse in size and shape, that have been shown to rapidly form highly ordered and microscopic 2D

‡ Present address: Celgard, LLC, 13800 South Lakes Drive, Charlotte, NC 28273, USA.
¶ Present address: HASYLAB at DESY, Notkestrasse 85, Hamburg, Germany.
§ Present address: Department of Physics, Soongsil University, Seoul 156-743, Korea.

superlattices on a subsecond to second time scale by convective assembly (Ashley *et al.*, 2011). Characterizing highly ordered systems like those described above exhibiting features spanning multiple length scales from <1 nm to macroscopic sizes requires a probing technique like high-resolution GIXS with statistically relevant large-footprint coverage over the surface. Moreover, determining the depth-dependence of the in-plane structures beneath the surface to a nanometer resolution, *e.g.* dispersion kinetics of nanoparticles in thin films, requires the use of X-ray waveguide-based grazing-incidence techniques (Narayanan *et al.*, 2005; Lee *et al.*, 2006; Jiang *et al.*, 2011) that require very high q resolution in the surface normal direction in addition to high in-plane q resolution. Finally, measuring the evolution of the time dependence of these processes in real time requires temporal resolution in addition to q resolution.

To accommodate these increasingly urgent needs, a GIXS facility has been constructed, successfully commissioned and operated as a side station, beamline 8-ID-E, of the dedicated undulator-based coherent X-ray photon correlation spectroscopy (XPCS) beamline, 8-ID, at the Advanced Photon Source (APS). Beamline 8-ID-E was designed with as few inserted optics as possible and so preserves the beam coherence while achieving the highest possible flux. The high coherence intrinsically enables a variety of structural characterization techniques that require high reciprocal-space resolution including film-based X-ray standing waves to probe depth dependence (Narayanan *et al.*, 2005; Lee *et al.*, 2006; Mukhopadhyay *et al.*, 2008), high-resolution GIXS for structures varying from nanometer to micrometer scales (Stein *et al.*, 2007*a*,*b*; Jiang *et al.*, 2010*b*; Ashley *et al.*, 2011), and XPCS for dynamics, as well as various combinations of these techniques (Narayanan *et al.*, 2007). In this paper we describe this dedicated beamline and provide a few examples of the exciting scientific results obtained from experiments performed there.

2. Design

2.1. Beamline overview

The 8-ID beamline, as schematically shown in Fig. 1(*a*), was designed for XPCS experiments where stability and preserving the X-ray wavefront are major design goals. The beamline is insertion-device-based and uses the radiation produced by APS undulator A. The typical operation energy is 7.35 keV (at the first harmonic). The 1σ source size is σ_x = 278 µm in the horizontal and σ_y = 9 µm in the vertical, with corresponding intrinsic beam divergences $\sigma_{x'}$ = 12 µrad and $\sigma_{y'}$ = 3.7 µrad, respectively. X-rays from the undulator propagate into the first optics enclosure (FOE) 8-ID-A, where the beam is reduced to 300 µm in diameter by a tapered pinhole. The pinhole reduces the transmitted power on the downstream optics without sacrificing useful coherent flux. The reduced power means the downstream white- and pink-beam optics (see below) only require gravity-fed water cooling, greatly improving the stability of the X-ray beam. A side-bounce mirror with selectable bare silicon, rhodium or platinum

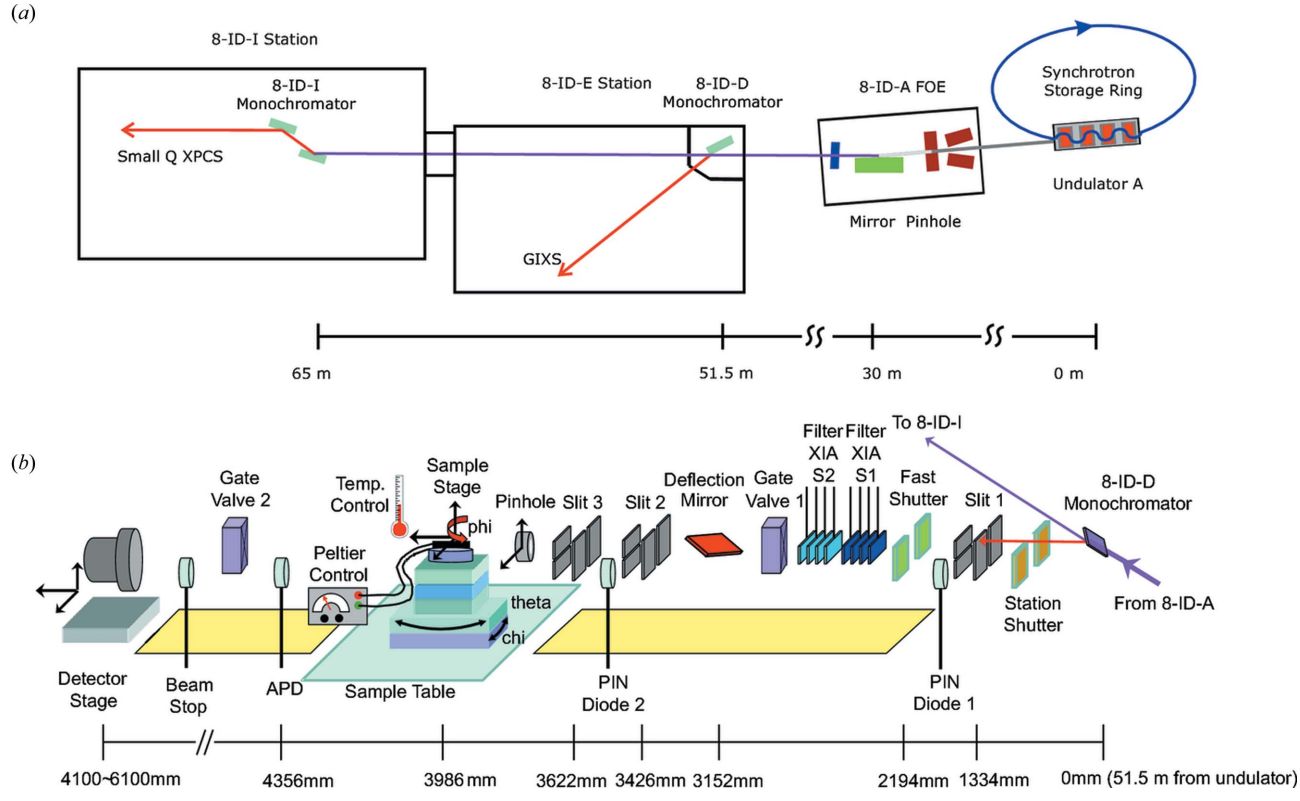

Figure 1
Schematics of the 8-ID beamline. (*a*) Sector overview and (*b*) the 8-ID-E GIXS branch.

stripes deflects the white beam inboard by 0.3°, delivering a so-called pink beam to the second optics enclosure (SOE) 8-ID-D. In the SOE, half of the pink beam is diffracted by a Si(111) single-bounce monochromator through a highly polished Be window into the 8-ID-E station. The undeflected half of the X-ray beam propagates downstream into the 8-ID-I station and is used for small-angle XPCS experiments. With only minimal high-quality optics being used prior to the beam entrance to the 8-ID-E station, the beam coherence is preserved. The transverse coherence lengths were measured to be ∼10 µm and ∼200 µm in the horizontal (H) and vertical (V) directions, respectively. Another key feature of the beamline is that the two experiment stations can be operated concurrently, maximizing the beam time available for GIXS without compromising XPCS operations. More detailed descriptions of the end-station 8-ID-I (not the subject of the paper) and the FOE and SOE can be found elsewhere (Sandy *et al.*, 1999, 2007; Narayanan *et al.*, 2008).

With respect to the side-bounce mirror in the FOE, the silicon stripe, with a critical energy of ∼12 keV, is the most commonly used stripe for the typical operation energy of 7.35 keV. Some experiments, however, such as liquid–liquid or liquid–solid interface scattering, require higher X-ray energies in order to reduce absorption and background scattering from the bulk liquid and the air. This is achieved by using the third undulator harmonic at 22.05 keV. To this end, the Rh stripe on the side-bounce mirror in the FOE is used at an incident angle less than its critical angle of Rh for 22.05 keV so that the third harmonic is deflected almost without loss. To block the first-harmonic component, a thin copper foil is inserted in the filter position.

2.2. GIXS set-up at 8-ID-E

Taking full advantage of the highly collimated undulator source, the dedicated GIXS beamline at 8-ID-E is designed with both simplicity and flexibility in mind to achieve high resolution in both reciprocal and real spaces as well as high temporal resolution. One aspect of its simplicity is that the photon energy is largely fixed ensuring high-throughput and user-friendly operation. On the other hand, the flexibility is provided especially with respect to sample positioning and sample environments. A diffractometer-based sample stage provides six degrees of sample motion and is large and robust enough to support many versatile sample environments. Another flexible feature is an adjustable sample-to-detector distance that allows q-range to be optimized to the problem at hand. The design is illustrated schematically in Fig. 1(*b*) and described in detail below.

2.2.1. Beam collimation. The optics set-up at 8-ID-E, with no wavefront disturbing focusing optics, makes it unique among most other X-ray scattering beamlines. The beam dimensions on the sample position are not achieved by focusing the incoming beam. Instead, they are defined using a series of precision in-vacuum upstream slits. Specifically, three sets of vacuum-compatible x–y slits (JJ X-Ray A/S) are employed upstream to define the incident beam size and to eliminate parasitic slit scattering. The first slit set (Slit 1) is placed 1334 mm away from the single-bounce monochromator and is usually used to define the beam size. The second and third sets (Slits 2 and 3) at 3426 mm and 3622 mm, respectively, away from the monochromator serve as guard slits to reduce parasitic slit scattering. All three slit sets are equipped with intelligent motor systems with micrometer precision. There is also a motorized pinhole (with exchangeable dimensions from 20 µm to 1 mm) mounted just prior to the sample position to reduce air background scattering if the sample environment is in air. The typical beam size ranges from 2 µm × 2 µm to 300 µm × 300 µm (H × V) depending on experimental needs. For coherent surface experiments, in order to reduce the spreading owing to Fraunhofer diffraction, Slit 2 is usually used to define the beam size at an opening smaller than or comparable with the transverse coherence lengths. For most GISAXS and GIWAXS experiments the beam size is typically set at 100 µm × 50 µm (H × V) with Slit 1 and the guard Slits 2 and 3 optimized at ∼140 µm × 100 µm and ∼200 µm × 150 µm, respectively. With these GISAXS/GIWAXS slit settings the flux at the sample position is $\sim 9 \times 10^{10}$ photons s^{-1} at 7.35 keV, and the geometric divergences are 7.5 µrad × 0.6 µrad (H × V). The overall divergences arising from geometric and intrinsic source contributions are then estimated to be about 14 µrad × 4 µrad (H × V), or 1.2×10^{-3} nm^{-1} and 3×10^{-4} nm^{-1} in terms of q in the horizontal and vertical directions, respectively. The net effect of the three-slit arrangement is to preserve the beam quality to be highly collimated, while maintaining sufficient coherent flux for most sample systems. The well collimated parallel beam enables analyzer-free high-resolution experiments that cannot be easily performed elsewhere, such as X-ray waveguide experiments and time-resolved high-resolution small-angle or wide-angle scattering experiments. In addition, the minimal X-ray optics ensure that the coherence of the beam is not degraded, enabling coherent experiments such as surface XPCS.

2.2.2. Sample environment. To perform high-resolution surface experiments, precise control of sample position and angle is critical. To this end, a customized diffractometer-based double-tilt Huber stage with xyz and rotation stages stacked on top is placed atop a six-degrees-of-freedom vibration-free sample table. This arrangement provides complete control of the positioning of the sample as is necessary for surface alignment, reflectivity and GIXS.

To meet the demands of various types of sample environment, several sample chambers were designed and commissioned. One of these is a small vacuum chamber that is directly integrated into the beamline with flexible vacuum bellows so that the beam path from the Be window after the monochromator in the SOE to the beam stop in front of the area detector is free of windows. The windowless set-up eliminates possible window-related parasitic scattering as well as the background scattering from the air path. Temperatures from 253 K to 503 K with <0.01 K accuracy are provided by high-accuracy heating and cooling elements composed of cartridge heaters, a Peltier device and a chilled-liquid base, and the

control is provided by a Lakeshore 340 temperature controller. In addition, a high-vacuum-compatible 360° rotation stage can be installed in the chamber for experiments that require both vacuum and full rotation range such as grating diffraction.

Other sample environments include a solvent chamber with separate temperature controls for the sample, solvent vapor and reservoir for solvent annealing experiments, and a Langmuir trough with an active vibration-isolation stage for liquid-surface scattering experiments. These two chambers require the vacuum path to be broken before and after the sample position, where a single-crystal mica window and a Kapton window are installed for the upstream and downstream vacuum paths, respectively. Finally, even though our set-up is not a specialized liquid-surface scattering beamline, the beam can be tilted down for liquid-surface GIXS experiments *via* a single-bounce mirror [Pt(30 nm)/Cr(5 nm)/Si] installed 834 mm upstream of the sample followed by corresponding offsets of slit sets 2 and 3 and the sample-stage elevator. This enables liquid-surface GIXS in an incidence-angle range of 0–1.8°.

2.2.3. Detection. An avalanche photodiode (APD), attached to a linear high-precision motorized vacuum feed-through located 370 mm downstream of the sample position, is used for sample alignment as well as reflectivity measurements up to a 2θ angle of 4°. With negligible beam divergence and a 5 mm × 0.3 mm (H × V) slit mounted on the front face of the APD, the reflectivity can be measured with such a high resolution that films of thicknesses up to 1 μm can be resolved. This enables a precise determination of the depth-dependent structure in thin films using thin-film-based X-ray waveguide effects (Wang *et al.*, 1991, 1992; Narayanan *et al.*, 2005; Hu *et al.*, 2006; Lee *et al.*, 2006; Mukhopadhyay *et al.*, 2008).

The exit flight path is immediately downstream of the sample. It is a vacuum path constructed from small sections of NW160 flanges that allow the sample-to-detector distance to be varied from 100 mm to 2100 mm. Therefore, at the standard energy of 7.35 keV, the accessible q-range varies from 0.01 to 20 nm^{-1}, corresponding to a real space length scale of 0.3 to 600 nm. At the downstream end of the exit flight path immediately before the last Kapton window an aluminium beam stop, 3 mm × 6 mm × 100 mm (W × D × H), wrapped in lead foil, and optionally topped with a 1 mm × 1 mm × 15 mm (W × D × H) single crystal of tungsten, is mounted vertically on the linearly motorized vacuum feed-through to prevent the direct beam, specular beam and strong diffuse scattering from hitting the area detector mounted at the end of the beamline.

One of several possible area detectors is mounted immediately downstream of the exit flight path. For GIXS, typical area detectors include a high-speed version of Pilatus 1M and a MAR165. A Coolsnap HQ^2 or a PI-LCX CCD are used for coherence-based experiments. As for the time resolution, the achievable frame frequency can be as high as 20 Hz with a millisecond shutter (Azsol GmbH) installed upstream, or 135 Hz in shutter-free continuous illumination mode with the fast-option Pilatus 1M camera.

2.3. GIXS data processing and analysis

To enhance the productivity of both more and less experienced users, the beamline has developed a number of *Matlab*-based software packages for on-site and post-experimental data processing. The packages provide features such as image correction, and data visualization and reduction.

In addition, the beamline also supports comprehensive data analysis and modeling. Proper modeling of GIXS data often requires use of the distorted-wave Born approximation (DWBA) in the GIXS geometry (Sinha *et al.*, 1988). In the early days of GIXS, analysis was often only performed in a qualitative manner, whereby only scattering peak positions and widths were identified. Recently, more quantitative analysis models have been developed using various DWBA derivatives applied to a variety of systems (Renaud *et al.*, 2009). Most of these models were developed for either single-layer films (Lee *et al.*, 2005; Tate *et al.*, 2006) or supported nano-islands (Rauscher *et al.*, 1999; Lazzari, 2002). While these analysis models are a step forward, they may not be precise when the nanostructures of interest significantly perturb the scattering potentials or when the size of the nanostructures is comparable with the length scale of the electric field intensity (EFI) distribution variation within a film. Accordingly, we have developed a general multi-layer DWBA theory for GIXS analysis, which can be applied to particles of arbitrary size, shape and distribution buried in a thin film (Jiang *et al.*, 2011). Our method self-consistently allows for the average perturbing effect of the buried particles on the EFI depth distribution and thus, in principle, yields the most accurate description of the scattering data. To assist the user community to more deeply and quantitatively understand the nanostructures they have measured, we have developed flexible analysis routines based on this general DWBA theory. The routines are provided to users and supported on a collaborative basis.

3. Commissioning and operations

The dedicated GIXS beamline has been successfully commissioned and is now operated for the APS user community. Commissioning was accomplished by performing various grazing-incidence experiments including, but not limited to, GISAXS, GIWAXS, GID (grazing-incidence diffraction), film-based XSW and surface XPCS. The detailed beamline capabilities are best illustrated by the several examples described below.

3.1. Scattering geometry

The convention for wave vector transfers, as implemented at 8-ID-E, is illustrated in Fig. 2. The incident- and exit-wave vectors are k_i and k_f, α_i and α_f are incident and exit angles, and 2θ is the in-plane scattering angle. The normal and in-plane components of the wave vector transfer are defined by

$$q_z = k_f \sin\alpha_f + k_i \sin\alpha_i, \quad (1)$$

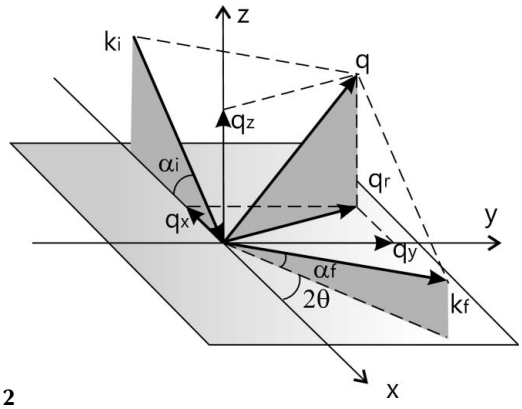

Figure 2
GIXS scattering geometry.

$$q_x = k_f \cos\alpha_f \cos 2\theta - k_i \cos\alpha_i, \quad (2)$$

$$q_y = k_f \cos\alpha_f \sin 2\theta, \quad (3)$$

$$q_r = \left(q_x^2 + q_y^2\right)^{1/2}. \quad (4)$$

3.2. X-ray standing-wave-based experiments

The advantage of a non-focusing coherent beamline is that very high reciprocal-space resolution can be achieved. This is essential for X-ray standing-wave (XSW) experiments, where waveguide-based resonance enhancement of the electric field is often used to extract depth-dependent structures (Wang *et al.*, 2001; Narayanan *et al.*, 2005; Mukhopadhyay *et al.*, 2008). X-ray standing waves are often created between parallel surfaces separated by a medium of a different electron density (Wang *et al.*, 1991, 1992; Feng *et al.*, 1993), *i.e.* a waveguide. The resonance modes in a thin-film-based X-ray waveguide are sensitive to the electron density profile of the film. At incident angles where resonance modes are created (resonant angles), the EFI of the XSW reaches its maximum at certain depths within the film, yielding an enhancement of the scattering from the structures at those particular depths by one to two orders of magnitude. Therefore, it is feasible to use the resonance enhancement to determine depth-dependent structure from GISAXS patterns (Narayanan *et al.*, 2005; Lin *et al.*, 2005; Lee *et al.*, 2006). This type of combined technique requires high reciprocal-space resolution to resolve the resonant angles in the direction normal to the film surface. A strict treatment of the resolution effect involves a consideration of the mutual coherence functions of the beam, as well as the electron density distribution of the sample (Sinha *et al.*, 1998). The effect of resolution on the creation of XSW has been discussed elsewhere (Jiang *et al.*, 2011). Using its highly collimated X-ray beam, 8-ID-E can readily achieve a resolution that is fine enough to resolve standing waves in films with thicknesses up to ~1 μm. For example, Fig. 3 shows a high-resolution reflectivity taken with X-rays of energy 7.35 keV from a polymer film of thickness ~800 nm on a silicon substrate. Here, the Kiessig fringes above the silicon critical angle, θ_c^{Si} = 0.245°, as well as the X-ray standing-wave oscillations between θ_c^{Si} and the polymer critical angle θ_c^{P} (grey region), are clearly resolved.

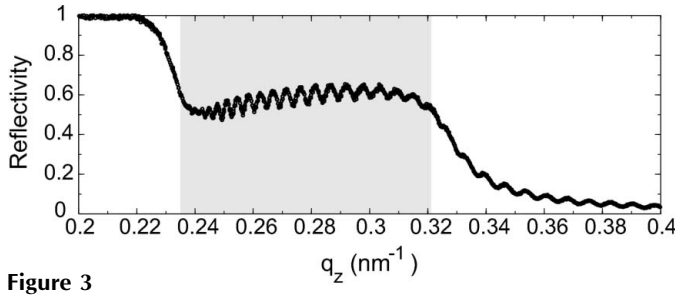

Figure 3
Reflectivity measured using an in-vacuum APD from a Si-supported polymer film of thickness ~800 nm. X-ray standing-wave oscillations are clearly resolved to a high resolution between the critical angles of the film and substrate (the shaded region).

Fig. 4 shows the feasibility of performing high-resolution GISAXS in the presence of XSW-based enhancement at 8-ID-E. Here the structure of a monolayer of gold nanoparticles 2–4 nm in diameter sandwiched between two poly(*tert*-butyl acrylate) (PtBA) films of equal thickness of ~85 nm has been investigated. The reflectivity in Fig. 4(*a*) indicates strong

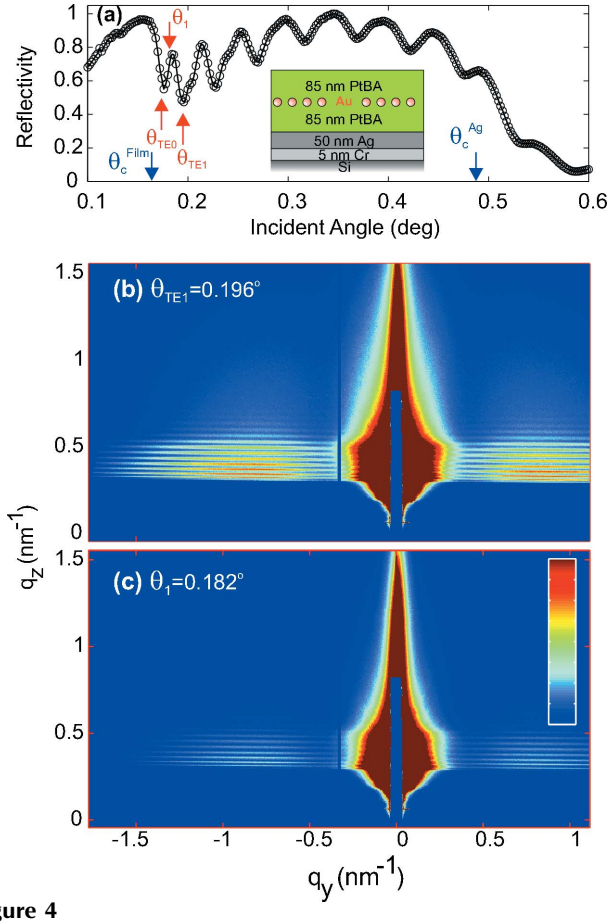

Figure 4
(*a*) Reflectivity from an as-deposited nanocomposite sandwich sample illustrated in the inset. θ_c^{Film} and θ_c^{Ag} are the critical angles for the film and the substrate, respectively. θ_{TE0} and θ_{TE1} are the first and second resonant angles, respectively. The first off-resonant angle, θ_1, is also labeled. (*b*) and (*c*) GISAXS patterns (displayed with identical intensity scales) measured at θ_{TE1} and θ_1, respectively.

intensity modulations between the critical angles of the PtBA film (θ_c^{Film}) and the Ag mirror (θ_c^{Ag}), and hence the existence of the waveguide-induced resonance enhancement. At an incident angle equal to the resonant angle at $\theta_{TE1} = 0.196°$, the scattering intensity from the nanoparticles is greatly enhanced (Fig. 4*b*) as compared with the off-resonant angle at $\theta_1 = 0.182°$ (Fig. 4*c*). In addition, the high scattering intensity afforded by the XSW-based enhancement has led to successful experiments to understand nanoparticle kinetics and dynamics in thin-film samples, *e.g.* the normal and in-plane diffusions of the particles (Narayanan *et al.*, 2005, 2007).

3.3. GIXS from mesoscale structures

In general, high reciprocal-space resolution in GIXS experiments is accomplished by installing an analyzer before a point detector. An analyzer scan does not have the time resolution that is crucial for kinetic and dynamic measurements and is also an inefficient way to use undulator beam time. With the highly collimated beam available on the GIXS branch at 8-ID-E, sufficiently high reciprocal resolution is achieved without sacrificing the time resolution.

A demonstration of the exceptionally high resolution achievable at 8-ID-E has been performed with a supported $BiFeO_3$ nanodot array fabricated by e-beam lithography, as shown in Fig. 5(*a*). The diffraction from the array having 1 µm line spacing is observed up to the seventh order in the q_x direction and is only limited by the collection area of the detector (Fig. 5*b*). The rapid oscillations along the arc in Fig. 5(*c*) indicate that the line spacing can be measured with an in-plane (parallel to the sample surface and perpendicular to the X-ray incidence) resolution of approximately 10 µm which is close to the horizontal transverse coherence length of the beam. This high resolution provides a precise measure of the in-plane structures spanning several orders of magnitude in length scale from <1 nm to macroscopic length scales.

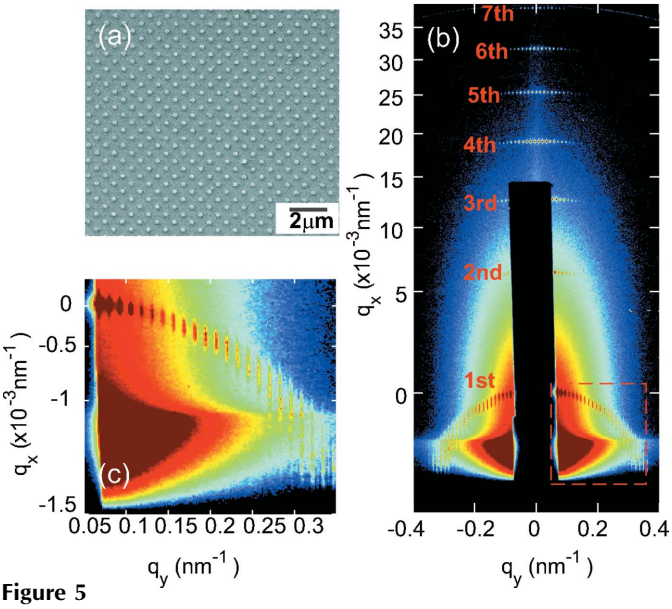

Figure 5
(*a*) Scanning electron microscope (SEM) image from a centered rectangular array of $BiFeO_3$ nanodots. Each nanodot is 200 nm in diameter and the array line spacing is 1 µm. (*b*) GISAXS pattern, with the boxed region magnified in (*c*). The diffractions from the in-plane spacing along the q_x direction are labeled for the first through seventh orders. As indicated in equations (1) and (2), and in Fig. 2, the vertical axis of the incident scattering plane (with in-plane scattering angle $2\theta = 0$) on the 2D area detector contains both q_x and q_z components that are related through $q_x = q_z \tan(1/2)(\alpha_i - \alpha_f)$. In typical GISAXS data, the q_x component is so small that this component is usually not of much interest for most samples. The q_x range covered in this experiment, however, is extremely revealing for the sample with very large ordered in-plane spacing between the features on a micrometer length scale. Therefore, q_x, instead of the ordinary q_z, is used to label the vertical axis.

3.4. High-resolution GISAXS of self-assembled systems

A typical example at 8-ID-E of high-resolution GISAXS applied to self-assembled systems is the structural characterization of 2D 'single-crystal' arrays consisting of nanoscopic micelles formed from the self-assembly of diblock copolymers on macroscopic hexagonal templates (Stein *et al.*, 2007*a*,*b*). Fig. 6(*a*) is the scanning electron microscope image of a silicon substrate patterned with hexagonal wells, spun-cast onto which is a poly(styrene-b-2-vinylpyridine) (PS-PVP) polymer film of 41 nm. Upon thermal annealing, the registration of the block copolymer to the patterned substrate leads to a monolayer of highly ordered PVP micelles that align with the edge of the well (Fig. 6*b*). GISAXS patterns (Fig. 6*c*) were recorded at an X-ray incident angle of 0.195° with the in-plane rotation angle Φ varying over a range of 80°. An intensity map $I(2\theta, \Phi)$ was then constructed by assembling the GISAXS line profiles for each Φ (Fig. 6*d*). Fig. 6(*e*) shows the $I(\Phi)$ line-cut for (10) diffraction. Fitting to a Fourier cosine series reveals long-range six-fold orientational order. To determine the positional order of the 2D superlattice, one needs to apply the Kosterlitz–Thouless–Halperin–Nelson–Young (KTHNY) theory, which states that, in a 2D system, quasi-long-range translational order is a signature of the 2D crystal phase (Nelson & Halperin, 1979). The width and the diffuse scattering associated with Bragg diffraction peaks from a 2D system yield the domain size (which is ∼1 µm on average for individual domains in the current example) and the degree of the translational order (Dutta & Sinha, 1981). Fig. 6(*f*) shows the (11) and (20) diffraction profiles. The power-law decay exponents of the diffuse scattering identify a 2D crystal phase for the micellar monolayer. Such area detector measurements would not be possible if the diffraction peak profile was dominated by the beam resolution rather than the intrinsic profile of the 2D crystal phase. Moreover such measurements would be incredibly inefficient with a point-detector-based analyzer set-up.

In addition to the high reciprocal-space resolution, we can take advantage of the time resolution afforded by the beamline to carry out *in situ* investigation of the self-assembly kinetics, *e.g.* evaporation-driven self-assembly of spherical gold nanoparticles into two-dimensional superlattices on the liquid/air interface (Narayanan *et al.*, 2004; Jiang *et al.*, 2010*b*). To identify the phases of the superlattices and the ordering behaviors during this process, one needs to perform quantitative line-shape analysis of the Bragg diffractions, *i.e.* the

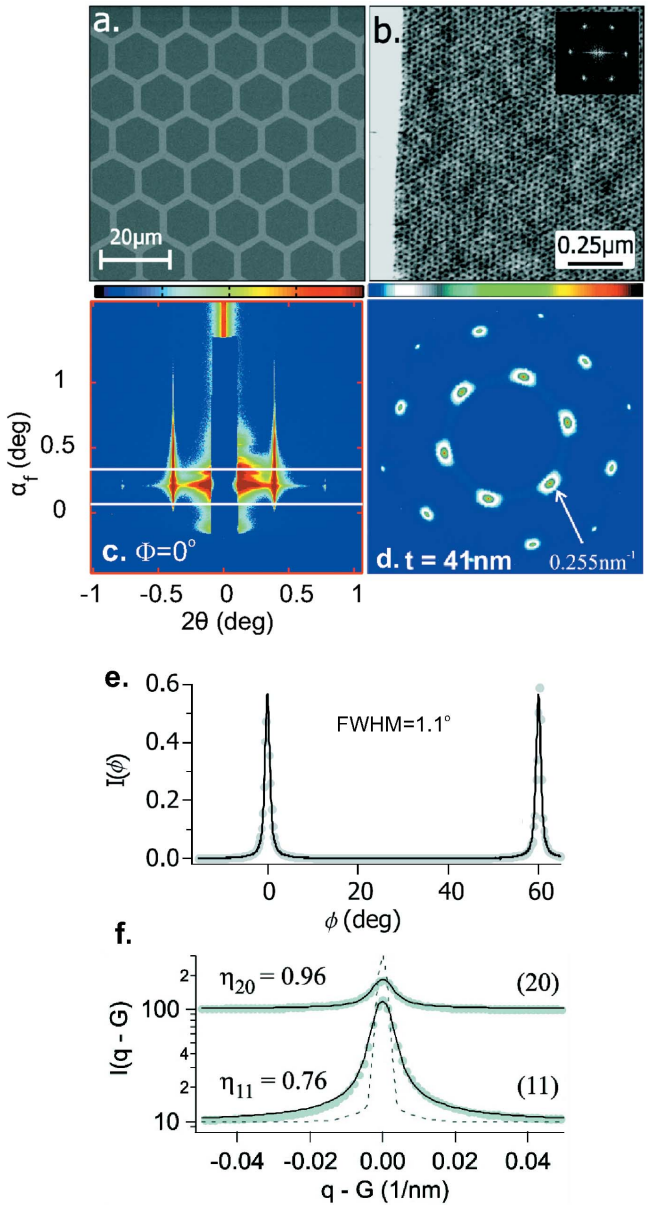

Figure 6
(*a*) SEM image of a hexagonally patterned silicon substrate. (*b*) Scanning force microscope image of the in-plane block copolymer structure adjacent to the edge of the confining well. (*c*) GISAXS pattern taken at an incident angle of 0.195° and an in-plane angle $\Phi = 0°$. (*d*) $I(2\theta, \Phi)$ constructed from the integrated line profiles like that defined by the two horizontal white lines shown in (*c*). (*e*) is a $I(\Phi)$ line-cut for the (10) diffraction. (*f*) shows the (11) and (20) in-plane diffraction profiles centered at the (11) and (20) peak positions. The dotted line is the resolution function. Figure adapted with permission from Stein *et al.* (2007*b*). Copyright (2007) American Chemical Society.

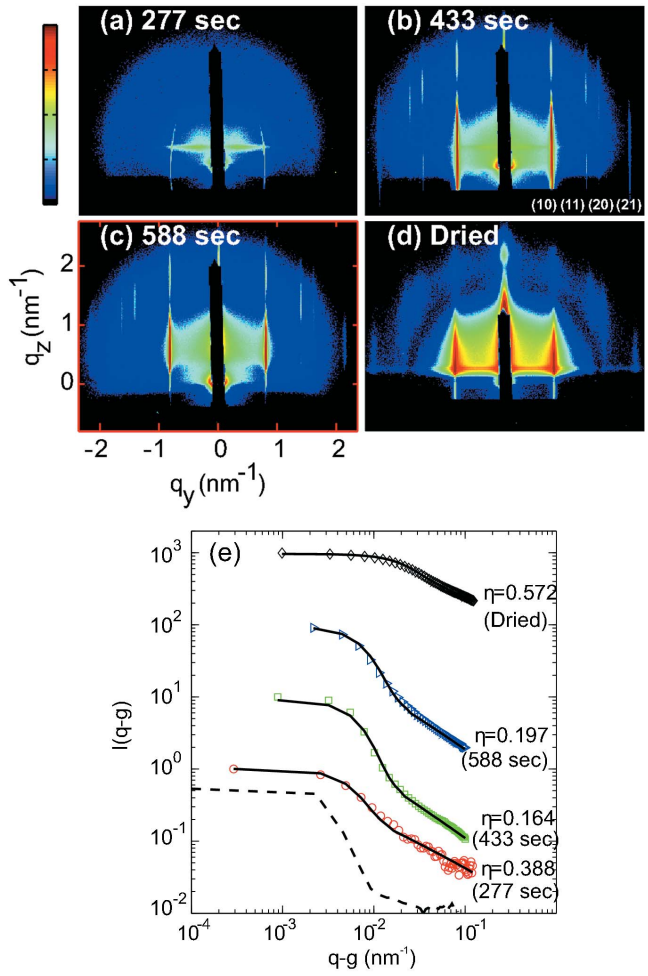

Figure 7
(*a*)–(*d*) *In situ* GISAXS patterns of 2D nanoparticle (d = 5.5 nm) superlattices at the liquid/air interface during the droplet evaporation. The exposure time for each image is 5 s. Diffraction orders (10), (11), (20) and (21) for the 2D hexagonal packing structures are labeled for 433 s in (*b*). (*e*) Horizonal line-shapes of the (10) Bragg diffraction with respect to g, the (10) reciprocal lattice vector. The dashed line represents the instrumentation resolution. Figure adapted with permission from Jiang *et al.* (2010*b*). Copyright (2010) American Chemical Society.

width of the Bragg diffraction tells the domain size and the decay exponent of the diffuse scattering carries information that can be used to determine the phase of a 2D lattice (Jiang *et al.*, 2010*b*). In the example shown in Fig. 7, by analyzing the line-shapes of the (10) Bragg diffraction, the scattering decay exponent η was obtained from the slope of the power-law decay of the diffuse scattering, $-1 + \eta$. The 2D superlattice was found to be in the crystalline phase with η less than the critical value of 1/4 for 2D hexagonal crystals (Nelson & Halperin, 1979) and the average domain size was ∼500 nm. The crystallinity, however, was destroyed upon complete drying as the decay exponent increases above the critical value. For the first time the crystalline phase of the 2D crystalline superlattice of nanoparticles was captured in action during its growth, providing invaluable information for the comprehensive understanding of the structural evolution in 2D nanoparticle superlattices. This type of experiment cannot normally be performed at beamlines with a focused beam. Typical focusing devices, such as X-ray mirrors, may increase the divergence, and thus worsen the resolution. Even with a 1:1 focusing ratio the devices can introduce excessive tail structures around the main beam owing to optical aberration and diffuse scattering. This may render the measurement of the diffuse scattering around the in-plane Bragg peaks impossible. Beamlines with an analyzer-based data collection scheme are not suitable either because of the lack of time resolution.

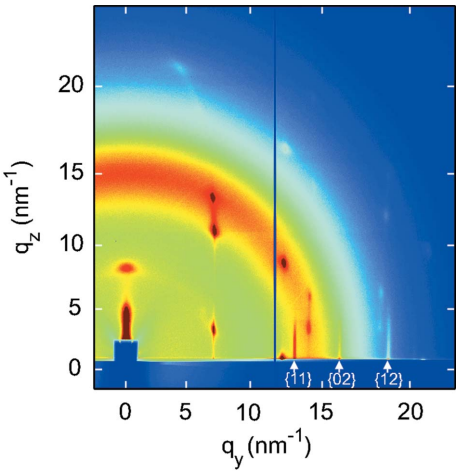

Figure 8
GIWAXS from an ambipolar OTFT on silicon. In-plane rod-like Bragg diffractions of the 2D ordered pentacenes are labeled. The other scattering features, *i.e.* the amorphous ring-like structures and the Bragg diffraction spots, arise from the partially ordered fullerene molecules.

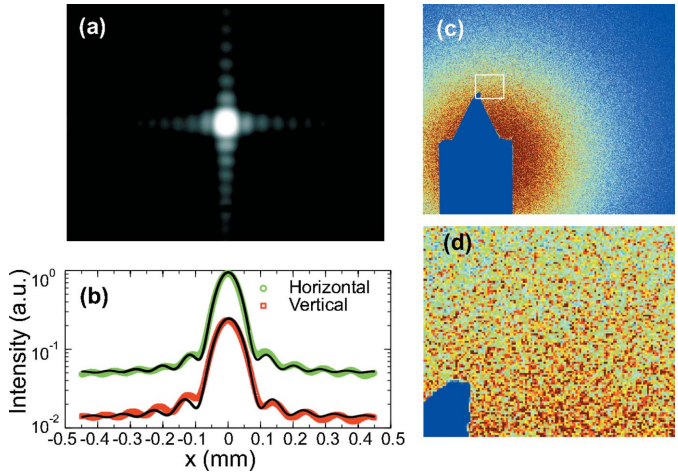

Figure 9
(*a*) Direct-beam diffraction pattern from Slit 2 (5 µm × 5 µm) measured on a Coolsnap detector mounted 2421 mm downstream from Slit 2. (*b*) Horizontal and vertical diffraction profiles through the center of the beam. Solid lines are calculations assuming a Fraunhofer single slit diffraction. (*c*) Static (averaged over 10 min) speckle pattern measured on aerogel with a partially coherent incident beam of 10 µm × 10 µm. (*d*) Magnification of the region marked in (*c*).

3.5. GIWAXS from supramolecular assemblies

Wide-angle scattering and diffraction experiments can also be carried out to near atomic resolution in the grazing-incidence geometry at 8-ID-E for the characterization of supramolecular assembled structures composed of small units, *e.g.* organic semiconducting molecules and biological molecules (Guo *et al.*, 2009; Liang *et al.*, 2009; Jiang *et al.*, 2010*a*; Rancatore *et al.*, 2010). Most GIWAXS experiments are resolution limited because of the beam divergence as well as the large vertical beam projection on the sample surface. Therefore, quantitative size characterization of fairly large domains (larger than tens of nanometers) becomes difficult (Mannsfeld *et al.*, 2009). At 8-ID-E, however, the beam is highly collimated so resolution is not compromised. Moreover, the beam size at the sample position can be reduced to as small as 5 µm with the high-precision slits. The GIWAXS capability at 8-ID-E is demonstrated in Fig. 8 where the scattering from an ambipolar organic thin-film transistor (OTFT) composed of a 9 nm layer of fullerene (C60) on a 1.9 nm layer of semiconductor pentacene derivatives supported by a silicon substrate is shown. Superimposed on the scattering of the amorphous fullerene structures, two sets of scattering patterns are observed arising from partially ordered fullerene and 2D pentacene supramolecular assemblies. With an incident beam size of 300 µm × 15 µm (H × V), incident flux of $\sim 8 \times 10^{10}$ photons s^{-1}, and a sample-to-detector distance of 208 mm, the in-plane reciprocal-space resolution is found to be 0.13 nm^{-1}, which means the resolvable size of crystalline domains is 48 nm.

3.6. Surface XPCS

High resolution can alternately be thought of as high coherence (Sinha *et al.*, 1998) implying that experiments demanding a coherent beam can be carried out at 8-ID-E. To demonstrate the coherence of the beam, the direct beam was measured through 5 µm × 5 µm upstream slits [Slit 2 in Fig. 1(*b*)] with a coherent flux of $\sim 5 \times 10^8$ photons s^{-1}. The scattering profile is shown in Fig. 9(*a*), where oscillations along the vertical and the horizontal directions arise from Fraunhofer diffraction. The slit diffraction intensity line profiles along the symmetry directions agree very well with the Fraunhofer single-slit diffraction calculations (Fig. 9*b*). With a coherent beam, the scattering from a sample with random spatial inhomogeneities does not resemble conventional SAXS with a smooth scattering profile. Instead, the scattering amplitudes within each coherent volume (defined as a region of size equal to the coherence of the beam) are summed up coherently, producing a speckled pattern, as shown, for example, in Figs. 9(*c*) and 9(*d*) for the coherent scattering from an aerogel sample. If the inhomogeneity in the sample fluctuates with time, the dynamics can be obtained by correlating the speckle intensities at various time delays, as in XPCS (Shpyrko *et al.*, 2007; Pierce *et al.*, 2009; Sanborn *et al.*, 2011). With the optimized GIXS set-up, surface XPCS is then feasible for resolving the fluctuations of surfaces and interfaces. This is demonstrated in Fig. 10 which shows the intensity–intensity autocorrelation function from a glycerol surface measured at $q_{\parallel} = 1.48 \times 10^{-5}$ nm with a 10 µm × 10 µm beam and using a Cyberstar scintillation detector. The solid line represents a fit to a single-exponential decay $g_2(t) = 1 + \beta \exp(-2t/\tau)$, where the characteristic decay time τ was found to be 0.35 ms. The corresponding coherent contrast β was 46% which is sufficiently high for coherent X-ray experiments.

4. Conclusions and prospects

Beamline 8-ID-E was constructed and commissioned as a dedicated coherent GIXS beamline at the APS. It has

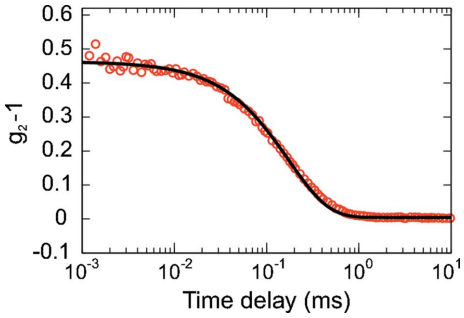

Figure 10
Intensity–intensity autocorrelation function measured at a wave vector transfer $q_{\parallel} = 1.48 \times 10^{-5}$ nm from liquid glycerol surface at room temperature.

demonstrated its high impact on nanoscience research by successfully delivering high-resolution, *in situ*, and real-time capabilities to the user communities.

The advantage of combining high resolution and surface sensitivity also enables the novel concept of lensless coherent surface scattering imaging. This new technique utilizes the enormously enhanced interference of surface structures near total external reflection, and has the promise of being able to reconstruct, *via* direct inversion of the scattered intensity, substrate-supported three-dimensional structures with a nanometer resolution (Sun *et al.*, 2012).

As for the future, within the framework of the APS Upgrade (the latest information regarding the APS Upgrade can be found at http://www.aps.anl.gov/Upgrade/), we anticipate an order of magnitude increase in the coherent flux as a result of the ring current and undulator upgrades. In addition, the large asymmetry in the transverse coherence lengths means that the beam may be focused vertically by implementing diffraction-limited focusing optics to maximize the usage of the coherent flux delivered by the undulator for surface experiments. This is expected to increase the coherent flux by another factor of ten at the sample position. Both of these upgrades will greatly facilitate coherence-based work as described above. Another future capability that will be enabled by the APS Upgrade is energy tunability which will be provided in the range 8–14 keV *via* use of a second diffraction-limited side-bounce mirror. Energy tunability will enable a number of additional capabilities such as grazing-incidence anomalous X-ray scattering experiments.

We thank Dr M. K. Mukhopadhyay for help in the surface XPCS experiment, Professor H. Kim at Sogang University for sharing GIWAXS results, Dr S.-H. Lee for engineering support, and H. Gibson and R. Ziegler for technical assistance. This work and use of the Advanced Photon Source, an Office of Science User Facility operated for the US Department of Energy (DOE) Office of Science by Argonne National Laboratory, were supported by the US DOE under Contract No. DE-AC02-06CH11357.

References

Ashley, C. E., Dunphy, D. R., Jiang, Z., Carnes, E. C., Yuan, Z., Petsev, D. N., Atanassov, P. B., Velev, O. D., Sprung, M., Wang, J., Peabody, D. S. & Brinker, C. J. (2011). *Small*, **7**, 1043–1050.
Dutta, P. & Sinha, S. K. (1981). *Phys. Rev. Lett.* **47**, 50–53.
Feng, Y. P., Sinha, S. K., Deckman, H. W., Hastings, J. B. & Siddons, D. P. (1993). *Phys. Rev. Lett.* **71**, 537–540.
Guo, J., Liang, Y., Xiao, S., Szarko, J. M., Sprung, M., Mukhopadhyay, M. K., Wang, J., Yu, L. & Chen, L. X. (2009). *New J. Chem.* **33**, 1497–1507.
Hu, X., Jiang, Z., Narayanan, S., Jiao, X., Sandy, A. R., Sinha, S. K., Lurio, L. B. & Lal, J. (2006). *Phys. Rev. E*, **74**, 010602R.
Jiang, Z., Lee, D. R., Narayanan, S., Wang, J. & Sinha, S. K. (2011). *Phys. Rev. B*, **84**, 075440.
Jiang, J., Lima, O. V., Pei, Y., Jiang, Z., Chen, Z., Yu, C., Wang, J., Zeng, X. C., Forsythe, E. & Tan, L. (2010*a*). *ACS Nano*, **4**, 3773–3780.
Jiang, Z., Lin, X.-M., Sprung, M., Narayanan, S. & Wang, J. (2010*b*). *Nano Lett.* **10**, 799–803.
Lazzari, R. (2002). *J. Appl. Cryst.* **35**, 406–421.
Lee, B., Yoon, J., Oh, W., Hwang, Y., Heo, K., Jin, K. S., Kim, J., Kim, K.-W. & Ree, M. (2005). *Macromolecules*, **38**, 3395–3405.
Lee, D. R., Hagman, A., Li, X., Narayanan, S., Wang, J. & Shull, K. R. (2006). *Appl. Phys. Lett.* **88**, 153101.
Liang, Y., Feng, D., Guo, J., Szarko, J. M., Ray, C., Chen, L. X. & Yu, L. (2009). *Macromolecules*, **42**, 1091–1098.
Lin, Y., Böker, A., He, J., Sill, K., Xiang, H., Abetz, C., Li, X., Wang, J., Emrick, T., Long, S., Wang, Q., Balazs, A. & Russell, T. P. (2005). *Nature (London)*, **434**, 55–59.
Mannsfeld, S. C. B., Virkar, A., Reese, C., Toney, M. F. & Bao, Z. (2009). *Adv. Mater.* **21**, 2294–2298.
Mukhopadhyay, M. K., Jiao, X., Lurio, L. B., Jiang, Z., Stark, J., Sprung, M., Narayanan, S., Sandy, A. R. & Sinha, S. K. (2008). *Phys. Rev. Lett.* **101**, 115501.
Narayanan, S., Lee, D. R., Guico, R. S., Sinha, S. K. & Wang, J. (2005). *Phys. Rev. Lett.* **94**, 145504.
Narayanan, S., Lee, D. R., Hagman, A., Li, X. & Wang, J. (2007). *Phys. Rev. Lett.* **98**, 185506.
Narayanan, S., Sandy, A., Shu, D., Sprung, M., Preissner, C. & Sullivan, J. (2008). *J. Synchrotron Rad.* **15**, 12–18.
Narayanan, S., Wang, J. & Lin, X. M. (2004). *Phys. Rev. Lett.* **93**, 135503.
Nelson, D. R. & Halperin, B. I. (1979). *Phys. Rev. B*, **19**, 2457–2484.
Park, S., Lee, D. H., Xu, J., Kim, B., Hong, S. W., Jeong, U., Xu, T. & Russell, T. P. (2009). *Science*, **323**, 1030–1033.
Pierce, M. S., Chang, K. C., Hennessy, D., Komanicky, V., Sprung, M., Sandy, A. & You, H. (2009). *Phys. Rev. Lett.* **103**, 165501.
Rancatore, B. J., Mauldin, C. E., Tung, S.-H., Wang, C., Hexemer, A., Strzalka, J., Frechét, J. M. J. & Xu, T. (2010). *ACS Nano*, **4**, 2721–2729.
Rauscher, M., Paniago, R., Metzger, H., Kovats, Z., Domke, J., Peisl, J., Pfannes, H.-D., Schulze, J. & Eisele, I. (1999). *J. Appl. Phys.* **86**, 6763–6769.
Renaud, G., Lazzari, R. & Leroy, F. (2009). *Surf. Sci. Rep.* **64**, 255–380.
Sanborn, C., Ludwig, K. F., Rogers, M. C. & Sutton, M. (2011). *Phys. Rev. Lett.* **107**, 015702.
Sandy, A. R., Jiao, X., Narayanan, S. & Sprung, M. (2007). *AIP Conf. Proc.* **879**, 898–901.
Sandy, A. R., Lurio, L. B., Mochrie, S. G. J., Malik, A., Stephenson, G. B., Pelletier, J. F. & Sutton, M. (1999). *J. Synchrotron Rad.* **6**, 1174–1184.
Shpyrko, O. G., Isaacs, E. D., Logan, J. M., Feng, Y., Aeppli, G., Jaramillo, R., Kim, H. C., Rosenbaum, T. F., Zschack, P., Sprung, M., Narayanan, S. & Sandy, A. R. (2007). *Nature (London)*, **447**, 68–71.
Sinha, S. K., Sirota, E. B., Garoff, S. & Stanley, H. B. (1988). *Phys. Rev. B*, **38**, 2297–2311.

Sinha, S. K., Tolan, M. & Gibaud, A. (1998). *Phys. Rev. B*, **57**, 2740–2758.
Stein, G. E., Kramer, E. J., Li, X. & Wang, J. (2007*a*). *Phys. Rev. Lett.* **98**, 086101.
Stein, G. E., Lee, W. B., Fredrickson, G. H., Kramer, E. J., Li, X. & Wang, J. (2007*b*). *Macromolecules*, **40**, 5791–5800.
Sun, T., Jiang, Z., Strzalka, J., Ocola, L. & Wang, J. (2012). Submitted.
Tate, M. P., Urade, V. N., Kowalski, J. D., Wei, T. C., Hamilton, B. D., Eggiman, B. W. & Hillhouse, H. W. (2006). *J. Phys. Chem. B*, **110**, 9882–9892.
Wang, J., Bedzyk, M. J. & Caffrey, M. (1992). *Science*, **258**, 775–778.
Wang, J., Bedzyk, M. J., Penner, T. L. & Caffrey, M. (1991). *Nature (London)*, **354**, 377–380.
Wang, J., Caffrey, M., Bedzyk, M. J. & Penner, T. L. (2001). *Langmuir*, **17**, 3671–3681.